A&A 403, 155–171 (2003)
DOI: 10.1051/0004-6361:20030257

Astronomy & Astrophysics

Tomography of a stellar X-ray corona: α Coronae Borealis⋆

M. Güdel[1], K. Arzner[1], M. Audard[2], and R. Mewe[3]

[1] Paul Scherrer Institut, Würenlingen & Villigen, CH-5232 Villigen PSI, Switzerland
e-mail: guedel@astro.phys.ethz.ch; arzner@astro.phys.ethz.ch
[2] Columbia Astrophysics Laboratory, Columbia University, 550 West 120th Street, New York, NY 10027, USA
e-mail: audard@astro.columbia.edu
[3] SRON National Institute for Space Research, Sorbonnelaan 2, 3584 CA Utrecht, The Netherlands
e-mail: r.mewe@sron.nl

Received 9 October 2002 / Accepted 12 February 2003

Abstract. We interpret the X-ray light curve obtained by *XMM-Newton* during a total X-ray eclipse in the nearby binary star α Coronae Borealis. This system consists of a G5 V main-sequence star orbiting an X-ray dark A0 star. The secondary G star is a young, active solar analog with an age of a few 100 Myr. As the primary A star eclipses active regions on the X-ray bright companion, the light curve drops in consecutive steps to zero; as individual active regions reappear during egress, the flux rises in similar steps. The ingress and egress light curves are combined to reconstruct the 2D distribution of X-ray brightness on and around the G star. Three different methods are applied, and variations due to statistical noise and uncertainties in the binary system parameters are discussed. Although the solutions are non-unique, all reconstructions reveal a similar distribution of X-ray bright regions and large areas with little flux. We present plausible estimates of (lower limits to) the electron densities in the bright regions, obtaining characteristic values between 10^9–3×10^{10} cm^{-3}.

Key words. stars: activity – stars: coronae – stars: individual: α CrB – X-rays: stars

1. Introduction

The Sun's magnetic activity has decayed considerably during its evolution on the main sequence; this trend can be followed in solar analogs of different ages across the electromagnetic spectrum (Dorren & Guinan 1994; Dorren et al. 1995; Güdel et al. 1997, 1998). Empirically, the total X-ray luminosity of main-sequence solar analogs depends on their rotation period, $L_{\rm X} \propto P^{-2.6}$ (Güdel et al. 1997 and references therein). The rotation period itself is an age indicator, at least for ages beyond ≈200 Myr for a G V star. However, while the enhanced magnetic activity of rapid rotators is attributed to an internal magnetic dynamo, it is not clear how a stellar corona attains its particular quiescent X-ray luminosity level. A stronger dynamo in more rapidly rotating stars may produce a larger surface magnetic filling factor, thus increasing the X-ray luminosity up to a maximum until the star is completely surrounded by active regions. This "saturation level" appears to occur at a rotation period of ≈2 d for a solar analog, corresponding to a ratio between X-ray and bolometric luminosities of $L_{\rm X}/L_{\rm bol} \approx 10^{-3}$ (Vilhu 1984; Vilhu & Walter 1987).

There are at least two problems with this interpretation. First, if the complete solar surface were filled with active regions, the maximum quiescent X-ray luminosity would reach ≈2×10^{29} erg s^{-1} (Vaiana & Rosner 1978), no more than ten percent of the maximum observed $L_{\rm X}$ of solar analogs (Pallavicini et al. 1981; Walter 1981). The additional luminosity may be due to a larger coronal height, or to larger densities since $L_{\rm X} \propto n_{\rm e}^2$ ($n_{\rm e}$ is the electron density). Recent X-ray spectral measurements using He-like line triplets consistently show high electron densities in magnetically active main-sequence stars even during quiescence, with $n_{\rm e} > 10^{10}$ cm^{-3} (Güdel et al. 2001a,b; Ness et al. 2001). Second, not only is the luminosity of more rapidly rotating solar analogs higher, but the characteristic temperature of the coronal plasma also rises with $L_{\rm X}$, roughly as $T \propto L_{\rm X}^{1/4.5}$ (Güdel et al. 1997). This is not expected if the filling factor is the only relevant parameter. Similarly, however, it is known that solar active regions are on average hotter than quiet regions (e.g., Peres et al. 2000), and hotter regions appear to reveal higher electron densities (Landi & Landini 1998 and references therein). The Sun during its activity cycle imitates part of the evolution of a solar analog in terms of surface coverage of magnetic fields, coronal temperature, and coronal density (e.g. Ayres 1997). It has been suggested that part or all of the observed stellar X-ray luminosity is due to an unresolved sequence of superimposed flares that occur at many sites in the tangled coronal magnetic fields, a hypothesis that is supported by theoretical arguments (Parker 1988) and by observations (Butler et al. 1986; Audard et al. 2000; Kashyap et al. 2002; Güdel et al. 2003). A larger coverage of the stellar surface with magnetic fields not only implies more coronal volume containing hot plasma in closed

Send offprint requests to: M. Güdel,
e-mail: guedel@astro.phys.ethz.ch

⋆ Based on observations obtained with XMM-Newton, an ESA science mission with instruments and contributions directly funded by ESA Member States and the USA (NASA).

magnetic fields but also a higher flare rate due to a larger rate of interactions between the tangled magnetic fields (Güdel et al. 1997). Flares, in turn, produce denser plasma through chromospheric evaporation, and a larger flare rate on average produces larger flares, resulting in higher temperatures as well (Feldman et al. 1995). Numerical calculations of statistical "microflare" models indeed compare favorably with global observables from stars such as light curves (Kopp & Poletto 1993) or emission measure distributions (Güdel et al. 1997).

A clear understanding of stellar coronal structure, however, requires techniques that reveal spatial information explicitly. There has been considerable progress in resolving stellar magnetospheric structures using very long baseline interferometry methods at radio wavelengths. Large magnetospheres predominate in tidally interacting close binaries, with diameters similar to the respective intrabinary distance (Mutel et al. 1985, 1998; see also Lim et al. 1996; Gunn et al. 1997). Late-type main-sequence active M dwarfs reveal structures with sizes up to several times the stellar diameter (Benz et al. 1995, 1998). No active solar analog has yet been resolved by VLBI techniques. It is generally unknown whether radio structures are co-spatial with X-ray coronae, since high-energy particles attain maximum life times in the low-density, low-magnetic field outer regions of the stellar atmosphere, while the X-rays originate predominantly from compact sources closer to the stellar surface where the electron density n_e is high.

Rotational modulation seen in X-ray or extreme-ultraviolet light curves may provide some information on location and extent of active regions, although time scales of up to several days and intrinsic variability mostly on shorter time scales put severe limitations on this method (for examples, see Drake et al. 1994; Güdel et al. 1995; Kürster et al. 1997; Audard et al. 2001). X-ray eclipses in binary stars provide spatial information on shorter time scales. In most cases, both binary components are X-ray sources. Examples include active binaries of the RS CVn type and main-sequence binaries (White et al. 1990; Siarkowski 1992; Siarkowski et al. 1996; Preś et al. 1995; Güdel et al. 2001b). Very few binaries are accessible to X-rays in which only one of the stars is active. Ideally, the eclipsing star is X-ray dark and produces a total stellar eclipse. The distribution of X-ray bright active regions on the eclipsed star should then map uniquely onto the observed light curve as bright areas disappear behind the dark eclipsing limb during eclipse ingress, and reappear during egress. The system considered in this paper, α CrB, belongs to this class. It is sufficiently X-ray bright to produce a detailed ingress and egress light curve.

The outline of the present paper is as follows: we describe our target in Sect. 2 and present the observations in Sect. 3. Section 4 discusses our image reconstruction algorithms and the results. Sections 5 and 6 discuss further aspects of our observations, and Sect. 7 presents our conclusions.

2. The target: α Coronae Borealis

The target of our observations, α CrB, is a binary consisting of an A0 V primary and a G5 V secondary in an eccentric ($e = 0.37$) orbit with a period of 17.3599 d (Tomkin & Popper 1986 = TP86). Its distance from the Sun is 22.9 pc (Perryman et al. 1997). The optical secondary eclipse is total even if the system inclination to the line of sight is only $i = 88.2°$ (the offset from 90° is in fact a pivotal advantage for our image reconstruction as will be discussed below). Its X-ray luminosity, $L_X \approx 6 \times 10^{28}$ erg s^{-1} (Schmitt & Kürster 1993), exceeds the typical L_X of the active Sun by a factor of 30 and is compatible with a stellar age of about 500–600 Myr if an X-ray decay law starting from a fast rotator on the Zero-Age Main Sequence is assumed (Güdel et al. 1997). Evolutionary calculations for the primary A star suggest an age of only 200–400 Myr, compatible with the possible membership in the Sirius Moving Group as inferred from its space motion (TP86). The upper limit to the secondary's equatorial rotation velocity of $v \sin i = 14$ km s^{-1} (TP86) implies, for a radius of 0.9 $R_\odot$ (TP86), a rotation period of at least 3.3 d (assuming $\sin i = 1$ for the inclination of the star's rotation axis), while its value of L_X suggests – assuming the validity of the activity-rotation relationship – a rotation period of about 7–9 days (Walter 1981; Güdel et al. 1997). The rotation is thus most likely not synchronous with the orbital motion. In any case, it is important to note that the displacement of coronal features on the G star due to rotation is small during our observations.

The α CrB system has previously been observed in X-rays by ROSAT. The secondary eclipses reveal no residual flux from the A star, as expected (Schmitt & Kürster 1993). The latter authors used one of the eclipse observations to reconstruct a rough surface X-ray map, applying a maximum likelihood method based on an optimization process by simulated annealing. The resulting map revealed a patchy surface coverage of X-ray emitting material. The few bright areas are reminiscent of solar active regions in size and distribution. Since the geometry was approximately revealed, lower limits to the electron density were estimated for one of the regions, $n_e \gtrsim 2 \times 10^{10}$ cm^{-3}. The reconstruction method was based strongly on statistical arguments since the intermittency of ROSAT's observing mode (a cycle of approximately 30 min on source followed by 60 min in the Earth shadow) and the low signal-to-noise ratio in the light curve prohibited individual identifications of active regions disappearing and reappearing as the eclipse proceeded. In a later paper (Schmitt 1998), additional ROSAT X-ray eclipses were presented, the main purpose being an X-ray determination of the apsidal motion in the system; the latter results in an advance of the periastron such that the time P_s elapsed between two secondary eclipses is longer than the period P_p between two primary eclipses (Volkov 1993). Schmitt (1998) found a marginal result, pointing to a difference between the secondary and primary eclipse-to-eclipse periods of $P_s - P_p = 4.8 \pm 2.1$ s, where the relativistic contribution is 0.95 s. We will report in Sect. 5 about our attempts to improve on this result.

3. Observations

We observed two secondary eclipses of α CrB with *XMM-Newton* (Jansen et al. 2001) as part of the *Reflection Grating Spectrometer* guaranteed time program; the observing log is given in Table 1. We made use of the data from the two EPIC MOS (Turner et al. 2001) cameras, and the EPIC PN camera (Strüder et al. 2001). The Reflection Grating

Table 1. Observing log.

	First observation: 2001 *January* 13	
Instrument	UT range	JD 2 451 923.0+
pn	16 : 22 : 55–22 : 56 : 56	0.18258–0.45620
MOS1	15 : 54 : 36–22 : 49 : 18	0.16292–0.45090
MOS2	15 : 55 : 21–22 : 49 : 18	0.16344–0.45090
	Second observation : 2001 August 27	
Instrument	UT range	JD 2452148.0+
pn	04 : 58 : 51–14 : 37 : 15	0.70753–1.10920
MOS1	04 : 43 : 16–14 : 15 : 25	0.69671–1.09404
MOS2	04 : 43 : 14–14 : 15 : 26	0.69669–1.09405

Spectrometers (RGS, den Herder et al. 2001) were operational as well, but the target is too faint to produce useful information in the high-resolution spectra. The Optical Monitor (OM, Mason et al. 2001) was turned off given the optical brightness of the system.

All EPIC cameras were operated in the small-window mode with the thick filter inserted in order to suppress the strong optical flux from the primary A star. To optimize the signal-to-noise ratio in the light curve and to suppress large background contributions and contributions from warm pixels in the very soft range, we extracted photons exclusively in the energy range 0.35–1.8 keV for the PN and 0.14–2.5 keV for the MOS cameras. X-ray photons were extracted using circular extraction regions centered on the star, with radii of approximately 20″ and 30″ for the MOS and PN cameras, respectively. A background light curve was extracted by combining photons from four areas on the outer CCD chips in each MOS (radii of approximately 50″; the small window does not provide sufficient source-free area for a background estimate). The background for the PN light curve was extracted from a circle with radius ≈80″ in a source-free field on the PN small window. We found that the combined background was very low during almost the entire observations. The average background level was 0.002 ct s^{-1} in an area equal to the source area in the PN camera, and similar for the MOS cameras. The induced statistical variation does not significantly affect the ingress and egress light curves; the only exception is for the final 18 min prior to the turn-off of the MOS cameras in the second observation. The turn-off occurred in response to increased background radiation levels when the satellite approached the Earth's outer radiation belt. Although the PN camera continued to observe for a short time, the light curve became unreliable, with several short-term spikes that we attribute to the rapidly increasing background level (competing with the source in count rate), while overall the flux stayed at a similar level as at the end of the MOS observations and as before the eclipse. A slight further increase by ≈15% in the high-background PN light curve may be possible, although this would result in a flux exceeding the pre-eclipse flux. Also, as the first observation shows (see below), the duration of the egress is entirely plausible as adopted. We therefore used the MOS and PN data only as long as all detectors were fully operational and will briefly return to this issue in our conclusions (Sect. 7). Various extractions in different energy bands assured us that the background subtraction is reliable until the end of this interval. The counts from the three EPIC detectors were combined and binned in time; an optimum time bin size of 300 s was adopted, sufficiently resolving flux gradients and at the same time providing a decent signal-to-noise ratio. All light curves were corrected to heliocentric dates.

The first observation partly failed due to problems with the acquisition of the guide star. Only the last part of the ingress, the total eclipse, and the complete egress were observed (Fig. 1, top), preventing us from reconstructing a 2D surface image of the star. The second observation covers the complete secondary eclipse (Fig. 1, bottom). The flux reaches pre-eclipse values around the time when the two MOS detectors were turned off.

We note two conspicuous features in the light curves: first, the gross shapes of the ingress and egress portions of the second light curve are asymmetric; the total ingress and egress durations are 2.6 and 1.75 hrs, respectively. And second, both during ingress and egress, a sequence of fast drops/rises in flux and several flux plateaus are evident. Also, the light curves from the first and the second observation are significantly different. We interpret the large gradients as active regions that disappear behind, and reappear from, the eclipsing limb of the A star. To check whether the light curves are contaminated by individual, outstanding flares, we produced hardness light curves (ratios between photon count rates above and below 1.2 keV, for example). X-ray flares on a star like α CrB are expected to last a few tens of minutes, and to produce hot plasma with hard emission during the early part of the flare. No significant features suggesting such events were found.

Although the EPIC X-ray spectra are of modest quality given the low count rates, a spectral fit to the PN spectrum (Fig. 2) provided some useful results. It is based on a spectral response matrix generated for the location and size of the extracted source area. The fit was performed in the XSPEC software using a single vmekal model (see Arnaud 1996 for details) with variable abundances of O, Ne, Mg, Si, S, and Fe. While Ne and S were not well constrained, O, Mg, Si, and Fe converged to similarly low abundances compared to solar photospheric values, namely 0.32 ± 0.08, 0.60 ± 0.18, 0.75 ± 0.40, 0.36 ± 0.04 times the corresponding values for the solar photosphere according to Anders & Grevesse (1989) (the errors are 1σ). The best-fit temperature was found to be acceptably robust, $kT = 0.45 \pm 0.03$ keV. We thus find a dominant electron temperature of 5 MK, compatible with other solar analogs of its activity level (Güdel et al. 1997), although the PN camera may miss some softer emission due to its insensitivity to emission below about 0.3 keV. The out-of-eclipse X-ray luminosity, evaluated between 0.1–10 keV for the best-fit model, was 5.6×10^{28} erg s^{-1}. This agrees well with the luminosity reported from ROSAT (Schmitt & Kürster 1993).

4. Image reconstruction

4.1. Basic parameters and geometry

The ingress and egress light curves contain information on the extent, the shape, and the location of various active regions

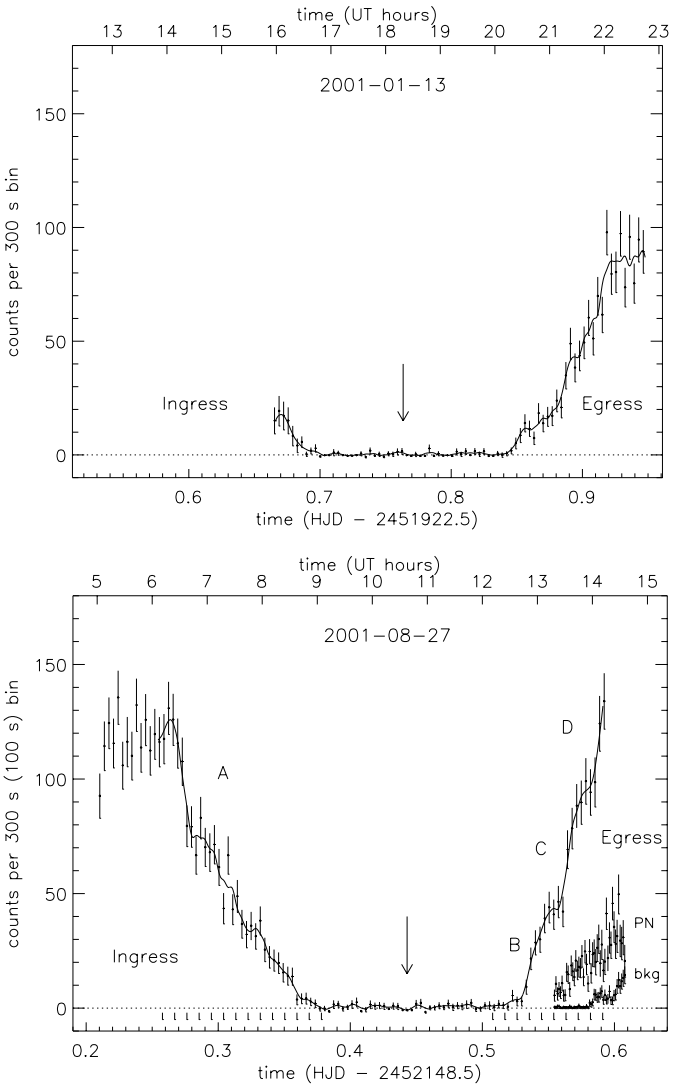

Fig. 1. The two X-ray eclipse light curves obtained by *XMM-Newton* on 2001 January 13 (top) and 2001 August 27 (bottom). All counts from the three EPIC cameras were co-added. (The initial 5 bins of the upper curve were observed by the MOS cameras only; we have scaled the count rate approximately to include the expected PN contribution, for illustration purposes.) The arrows indicate our adopted times of mid-secondary eclipse. The small grid given below the zero line in the lower panel indicates the time grid used for the CLEAN method described in Sect. 4.2. Note the strong asymmetry in the lower light curve, and the individual steep flux decreases and increases, labeled *A*, *B*, *C*, and *D* that are further discussed in Sect. 7. The solid line is a smoothed, near-monotonic version of the light curve. For the final part of the second observation, the PN count light curve (extending beyond the MOS observations) is shown separately in 100 s bins, illustrating the problematic development after 0.59 d due to rapidly increasing background radiation (curve labeled "bkg").

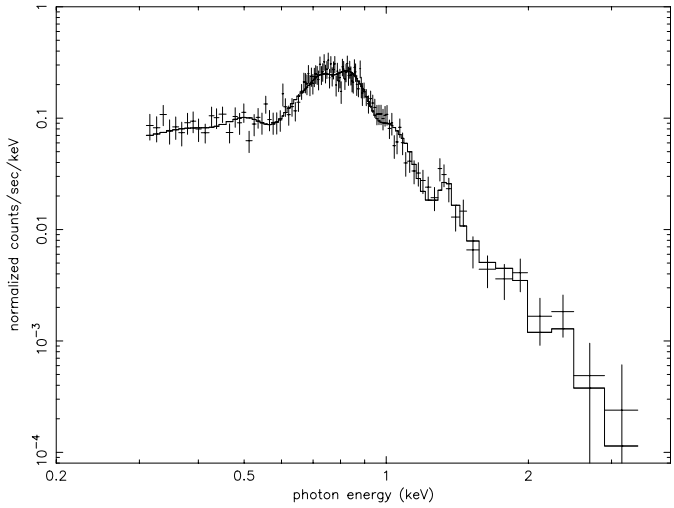

Fig. 2. EPIC PN spectrum and fit using one single vmekal component in XSPEC. All data collected during the pre-eclipse interval, during the ingress phase, and during the low-background egress phase before 0.58 d were used.

on the secondary G star. To reconstruct an eclipse map, the geometry of the system must be known with some accuracy. We adopted the binary orbital elements (a, e, i, ω) and the stellar radii (R_A and R_G) from TP86, allowing for some optimization within 1σ of the respective parameter. The original parameters are given in Table 2 together with our adopted values.

The geometry of the eclipse is shown in Fig. 3. The most critical values for the image reconstruction are those of the primary radius R_A, the orbit inclination against the line of sight *i*, and the time of periastron passage T_0. The value of T_0 fixes the time reference for the eclipse. The values given in the literature are subject to an error sufficiently large (≈40 min, see TP86) to result in ambiguities or inconsistencies. The ill-determined periastron advance adds to the problem. The goal, then, is to find the most likely center of the secondary eclipse at the epoch of observation, subject to the condition that all reconstructed X-ray features should be reasonably close to the disk of the G star. We used the formulae given by Meeus (1988) to calculate the projections of the two stars onto the sky at any given time (note that the angle of the ascending node is not required for our problem; for convenience, we use a value of 90°. The true value as found by Hipparcos is 330.4°, see Perryman et al. 1997).

Because T_0 can only be determined indirectly from optical observations (TP86) and the extrapolation to current dates is not accurate enough, we use the time of the secondary mid-eclipse as the principal time anchor (see below), and adjust the time of the periastron passage accordingly so that the mid-eclipse occurs at the right time as required by calculating the orbital positions of the stars using the given elements for the Kepler orbit. We briefly discuss the adopted values in the context of the geometry of the eclipse. As illustrated in Fig. 3, the primary star's limb projects circles as it moves in front of the secondary (which we hold fixed in the following). The different locations of the primary limb in this figure refer to a grid of times during the ingress (sample centered on the left side) and egress (sample centered on the right side), where the grid time step is 800 s (cf. Fig. 1). The slices between any two adjacent limbs describe the area across which the A star limb has moved during an 800 s interval. The adopted timing of the secondary

eclipse should guarantee that all observed X-ray sources can be located reasonably close to the secondary G star.

We thus adopted, for our second observation, a time of the mid-secondary eclipse only 293 s later than that predicted by using ROSAT eclipses reported earlier (see Table 2) in combination with the secondary period from Volkov (1993). (The difference is hardly significant as discussed further below – see Sect. 5.) This parameter set was found to allow all X-ray sources suggested from the ingress and egress light curves to be located within $\approx 1.25 R_{\rm G}$ of the center of the G star disk (see discussion below and in Sect. 4.7 for details on the choice of this limiting radius). It leads to a predicted mid-eclipse centered closely between the end of the X-ray ingress and the start of the X-ray egress as seen in Fig. 1b (and similarly for Fig. 1a). However, it is not centered between the beginning of the ingress and the end of the egress, due to the asymmetry of the light curve. If we had assumed a much earlier secondary mid-eclipse (i.e., a smaller T_0), then the bright source responsible for the final drop during ingress just before full occultation at 0.36–0.38 d would be located too far outside the G star limb. A much later mid-eclipse (larger T_0) is problematic as well: The bright source(s) associated with the first drop of the eclipse ingress (at 0.27–0.28 d) and with the first flux increase after full occultation (at 0.53–0.55 d) would fall too far outside the G star limb.

If we had adopted other values for T_0, then the location of the G star would be offset relative to the A star for any given time compared to the situation assumed here. The offset is characterized by the three vertical bars below the G star in Fig. 3. We fix the coordinate system and the A star locations for our adopted parameter set. The vertical bars then mark the locations of the secondary's central meridian at mid-eclipse if we had adopted (from left to right) (1) the time of mid-secondary eclipse T_0 from TP86 combined with the secondary period from Volkov (1993), (2) both parameters from Schmitt (1998) based on ROSAT X-ray eclipses without our 293 s time correction, while (3) represents our adopted values.

The radius of the A star determines the location where any pair of slices, one defined by an 800 s interval during ingress and one during egress, intersect (see Fig. 3). If $R_{\rm A}$ is too large, then the intersections tend to be too high above the projected orbital plane (large vertical displacement in vertical direction in Fig. 3); sources close to the plane are eclipsed for too long to be compatible with the observed eclipse duration. The orbit inclination i determines the vertical distance of the G star from the projected trajectory of the A star center. A larger value of i (within $0^\circ \le i \le 90^\circ$) puts the G star closer to the projected path of the A stars center and requires a smaller radius $R_{\rm A}$ to model the X-ray eclipse light curve. The deviation of i from 90° is in fact an advantage for our image reconstructions; if the projection of the G star fell onto both the northern (upper in Fig. 3) and the southern (lower) hemisphere of the A star, then there would be two intersections between several pairs of ingress and egress limb slices within 1.25 G star radii (our adopted limit), making the image reconstruction ambiguous with respect to the north-south symmetry. We have adjusted $R_{\rm A}$ to 0.95 times the value given in TP86, which is only a 0.5σ deviation but optimizes the reconstruction. Further, i was lowered by 0.1°, corresponding to a correction of 1σ, i.e., we adopt $i = 88.1^\circ$ instead of $i = 88.2^\circ$ as given by TP86.

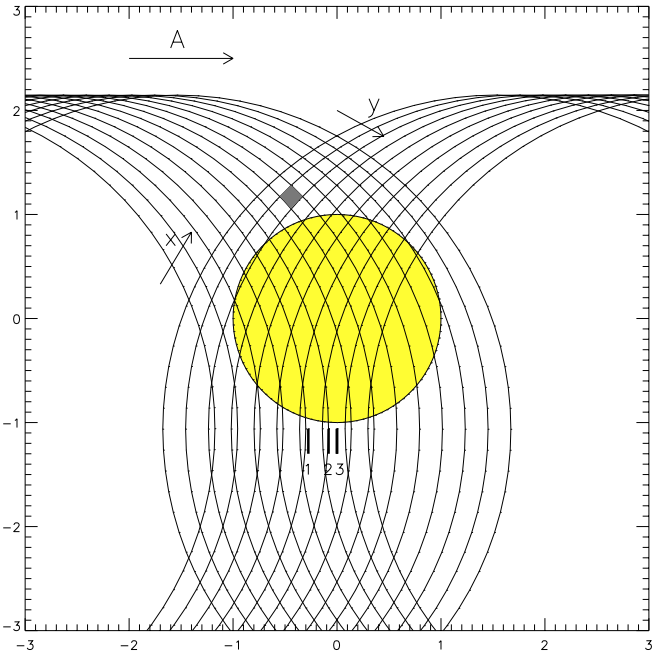

Fig. 3. Geometry of α CrB during the secondary eclipse. The large circles illustrate the limbs of the A star moving in front of the G star from left to right. The left set of limbs corresponds to the time bins in the ingress light curve used for the CLEAN reconstruction discussed in Sect. 4.2, while the right set corresponds to the egress bins. The three black bars below the G star indicate the position of the G star central meridian during times of mid-eclipse relative to the timing adopted here, for different orbit parameter sets discussed in the text. The pixel shaded gray is, as an example, located at coordinates $x = 8,\ y = 2$.

The maximum height of X-ray emitting material above the stellar surface is unknown. The pressure scale height can be calculated from

$$\Lambda = \frac{kT}{\mu m_{\rm H} g} \qquad (1)$$

where g is the surface gravity, $g = GM_{\rm G}/R_{\rm G}^2 = 3.1\times10^4$ cm s^{-2} using the secondary mass and radius from TP86, $G = 6.67 \times 10^{-8}$ cm^3 g^{-1} s^{-2} is the gravitational constant, $\mu \approx 0.67$ is the mean molecular weight, and $m_{\rm H}$ is the proton mass. We use $kT = 0.45$ keV as reported in Sect. 3. Then, $\Lambda \approx 0.33 R_{\rm G}$. Since the X-ray emissivity scales with the square of the electron density $n_{\rm e}$, 63% of the X-ray light is expected to originate from within $\Lambda/2$ above the surface. Magnetic fields can confine this radius further. To allow for detection of fainter material above the limb, we confined our image reconstruction to within $1.25 R_{\rm G}$ from the center of the G star. This also accounts for some uncertainty in the mid-eclipse time and the radius of the secondary. A radius of $1.25 R_{\rm G}$ is also sufficient to account for all sources that produce the ingress and egress light curves, i.e., the relatively long ingress light curve cannot map completely onto an area defined by a significantly smaller radius (see Sect. 4.7 for further discussion).

Table 2. Stellar system parameters.

Parameter	Literature Value	Reference	Adopted Value
A star radius R_A	$(3.04 \pm 0.30)\ R_\odot$	1	$2.89\ R_\odot$
G star radius R_G	$(0.90 \pm 0.04)\ R_\odot$	1	$0.90\ R_\odot$
Semimajor axis a	...	1	2.981×10^{12} cm[a]
Eccentricity e	0.370	1	0.370
Orbit inclination i	$88.2° \pm 0.1°$	1	88.1°
Longitude of periastron ω	311.0°	1	311.0°
Periastron passage T_0 (HJD)	2452149.7513	1	2452149.8278
Secondary mid-eclipse T_G (HJD)	2452148.9314	2	...
	2452148.9396	3	2452148.9430
Primary eclipse period P_A	17.35990 d	1	17.35990 d
Secondary eclipse period P_G	17.3599203 d	4	17.35996 d

References: (1) TP86, Table II, entry 4, using orbit period $P = 17.3599$ d.
(2) TP86 p. 1434 using $E = 1669.659205$, with the secondary minimum occurring at phase 0.659205 (as calculated from orbit elements), plus 1669 times 1.74 s per orbit for the secondary period due to apsidal motion as given by Volkov (1993).
(3) After Schmitt (1998), average derived from the four values of X-ray t_{mid} given in his Table 3, advancing them using $P_s - P_p = 4.8$ s as given in the same reference.
(4) Volkov (1993); adopted value from Schmitt (1998).
Note: [a] using Kepler's law with masses and orbit period as given in TP86.

4.2. Backprojection and CLEAN

We project sets of A star limbs onto the G star at a regular grid of times during ingress and during egress (Fig. 1), as shown in Fig. 3. The set of limb circles centered on the left side of the figure refers to ingress positions, while the set centered on the right side refers to egress positions. The two families of limbs define a grid of (non-rectangular) 2D pixels projected onto the G star and its environment. We identify pixels by two coordinates (x_i, y_j) where $x_i = 1, 2, 3...$ indicates the pixel "column" number defined by the ingress limbs, counting from left to right (along the arrow labeled x in Fig. 3) for increasing time, and y_j analogously refers to the pixel "row" number defined by the egress limbs (counting along the arrow labeled y). Pixel (x_i, y_j) is thus defined as the intersection of column x_i with row y_j. The pixel marked in gray in Fig. 3 is located at $x = 8, y = 2$, for example.

If we had observed only the ingress light curve, then a 1D image could be reconstructed as follows: The drop of flux within a time interval Δt corresponds to flux that, in the projection onto the sky, is located between the two A star limbs at the beginning and at the end of this time interval. This flux thus originates from a column at the corresponding value of x_i, but the distribution in the y_j rows (along the eclipsing limb) is unknown. Analogously, the egress light curve alone determines a 1D image in which flux is distributed among the rows with indices y_j, while the distribution in the x_i columns is unknown.

Since the ingress and the egress slices are oriented at largely different angles in the area of interest, the two 1D images contain complementary information on the 2D distribution of the X-ray bright material. The relevant problem is known in tomography, viz. the reconstruction of a 2D (or 3D) structure given projections onto different axes. The *Radon* backprojection (Radon 1917) is used to reconstruct an approximation to the original brightness distribution. The limiting case of only two independent projections is in general insufficient to obtain reliable information by backprojection alone. We therefore use a simple backprojection complemented by a CLEAN algorithm, as follows.

While the coordinate grid is distorted as illustrated in Fig. 3, we emphasize that this reflects the unequal amount of information from different regions on the secondary star. For the same observing time resolution, X-ray sources in the southern (lower) part of the secondary can be smeared out further than in the northern part to produce the same signal in the light curve. The coordinate system described here thus reflects the constraints available in different regions and introduces the least bias. The flux in any given pixel column at x_i is given by the difference of measured flux in the light curve at the beginning and at the end of the time interval. We produce a 1D image by uniformly distributing the flux at x_i across all acceptable y_j values ("backprojection from x along y"). We analogously backproject the differential fluxes in the egress light curve at any given y_j across all acceptable x_i values, co-adding them to the first backprojection values ("backprojection from y along x"; see Fig. 4 for a simulated example; note that the area of acceptable pixels in the real data is not rectangular as we additionally require the pixel *centers* to be located closer than $1.25R_G$ to the center of the G star in the plane of projection). The intersection of the brightest column x_i with the brightest row y_j defines the brightest pixel in the backprojection map at the location (x_i, y_j) and this pixel is likely to represent a true source on the star. We subtract a fraction g $(0 < g \leq 1)$ of the pixel brightness equally from all pixels in column x_i and in row y_j (thus

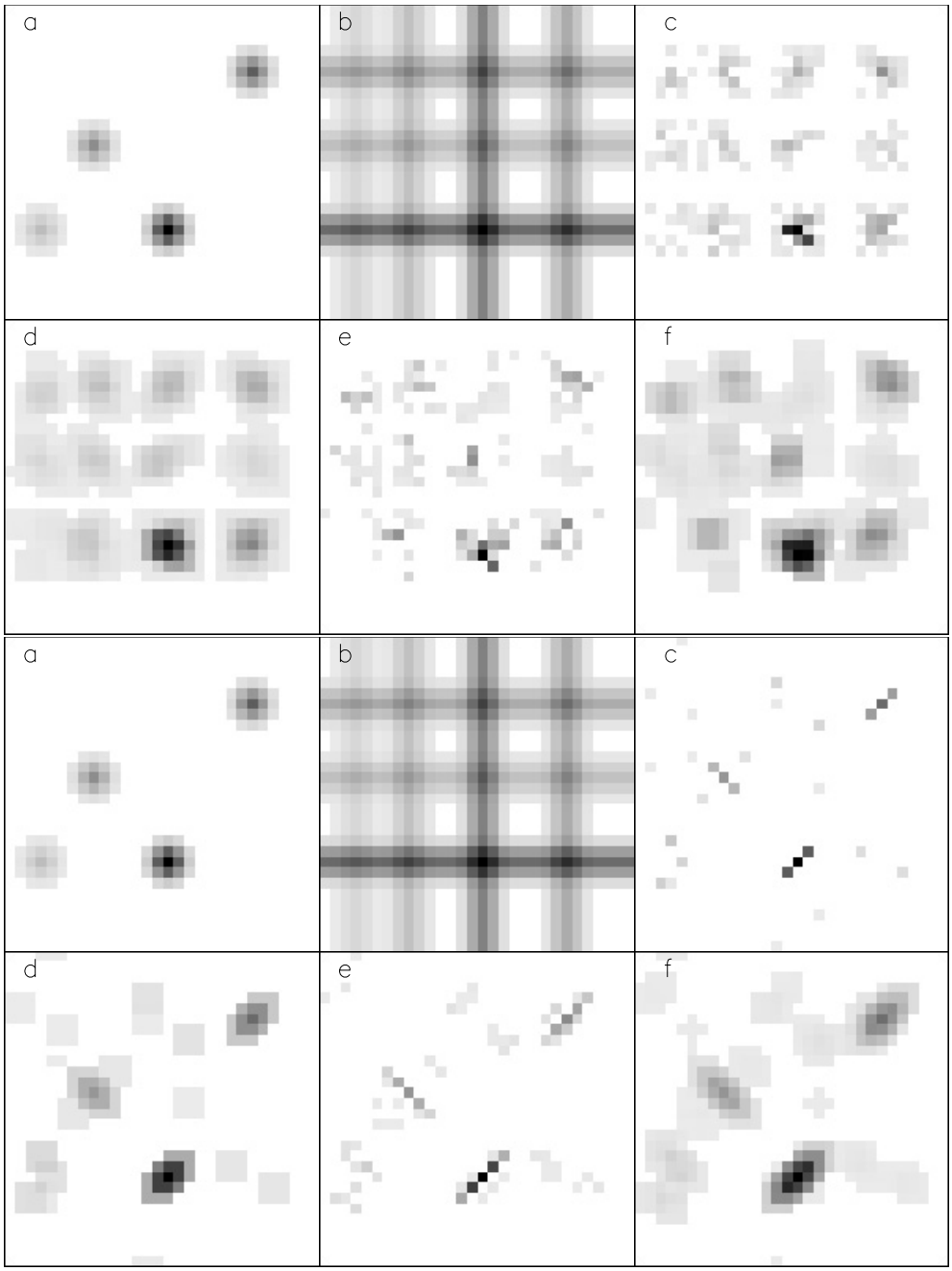

Fig. 4. Simulation of backprojection/CLEAN reconstruction algorithm using a CLEAN gain of 0.1 (upper set) and 0.5 (lower set). The individual figures illustrate **a)** the simulated map containing four 2D Gaussian sources, **b)** the backprojection map using the x and y projections of **a)**, **c)** the clean map, **d)** the same after smoothing with a 3×3 boxcar, **e)** the map resulting from applying a redistribution algorithm to map **d)**, and **f)** the same map after smoothing with a 3×3 boxcar. A gain of $g = 0.5$ recovers the original sources closely, while $g = 0.1$ produces too many scattered sources, although their shapes are similar to the original sources.

reversing part of the backprojection operation) and add the flux to pixel (x_i, y_j) on a clean map. This cleaning step is iterated using the residual backprojection map until all flux has been eliminated. The clean map then contains – after transformation to the bent coordinate system defined by the stellar limbs – a better representation of the true 2D flux distribution, where the quality of the clean map depends on the "gain factor" g.

Since CLEAN works on the flux differences within a time bin and the algorithm is rather sensitive to noise, we chose somewhat coarser bins than given in the light curve in Fig. 1 and used for the other two methods discussed below, providing complementary information on the large-scale X-ray features on the stellar surface. The original light curve was spline-interpolated to a larger number of bins, then smoothed such that nearly monotonically decreasing (for the ingress) and monotonically increasing (for the egress) light curve sections were obtained (Fig. 1). This smoothed light curve was then divided into 800 s bins by a regular time grid (defining our x_i columns for ingress and y_i rows for egress).

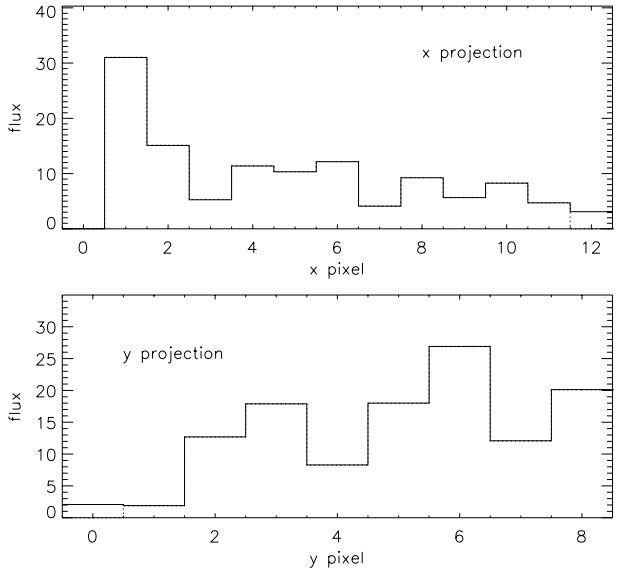

Fig. 5. Projections of the clean map of α CrB to x (upper panel) and to y (lower panel) using a gain of $g = 0.1$. The solid lines are the projections in the original light curve data (differences between fluxes at two consecutive time-grid points, see grid in the lower part of Fig. 1, bottom); the dashed histograms show the projections of the clean map.

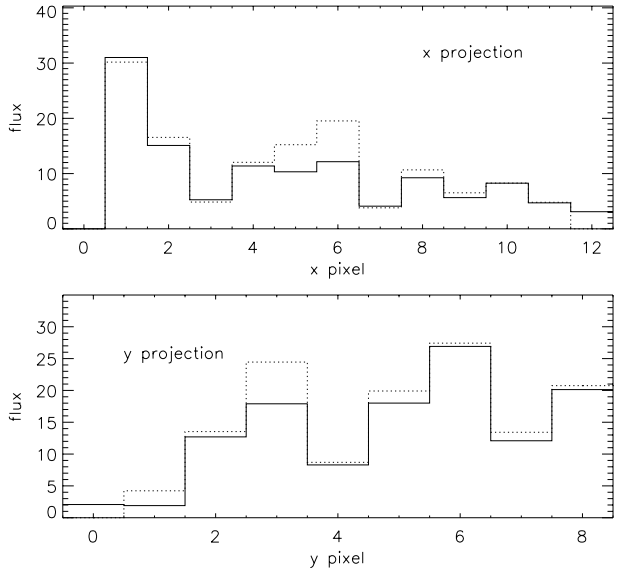

Fig. 6. Same as Fig. 5, but for a gain of $g = 0.5$.

We used simulations to assess the optimum value of g. From the light curve in Fig. 1, a small number of bright features is expected corresponding, e.g., to features *A*, *B*, *C*, and *D*. Our simulations used four 2D Gaussian sources on a rectangular 30×30 pixels grid, with relative brightnesses of 5, 3, 2, and 1, as illustrated in Fig. 4. We intentionally placed the strongest and the weakest source at the same y in order to investigate the effects of degeneracy in the projections (without overlapping source projections, an accurate reconstruction is trivial). A large g removes a large fraction of the flux of any suspected source at (x_i, y_j), attributing it to a single pixel in the clean map. Only few iterations are required to remove all flux from the backprojection map. As expected, the clean map tends to contain only few, well localized sources. However, the large removal of flux in a single iteration may subtract too much flux in some fainter pixels along x_i or y_j if multiple pixels have contributed to the flux at (x_i, y_j) during the backprojection operation; negative flux is thus produced in some areas although this will not further be considered for the clean map. These inconsistencies are frozen in the clean map, such that the projections onto the x and the y axis are not identical to the projections of the original map. A relatively large g is thus appropriate only for maps that are expected to contain few small sources where the brightest residuals in the residual maps are likely to correspond to true sources. In contrast, using a small g converges precisely to a map that has the same projections as the original map, but the solution distributes flux over large areas. The critical value of g that separates the two regimes was found to be between 0.4 and 0.5. The simulation shown in Fig. 4 (see figure legend for a description of the individual panels) profited from a large gain, $g = 0.5$, while a gain of $g = 0.1$ produced too many scattered sources, although their shapes are similar to the original sources.

We show the results of the backprojection/CLEAN inversion of our stellar data in Figs. 5–7 for gains of 0.1 and 0.5. Figures 5 and 6 show the projections of the map onto x and y, i.e., corresponding to the change of flux within the time bins of the ingress and the egress light curves, respectively. Whereas the low-gain option closely recovers the projection (Fig. 5, exceptions are small amounts of flux in the outermost bins that fall outside the formal limit of $1.25R_*$ but that are hardly significant), the high-gain solution reveals considerable deviations although the overall shape of the projections is correctly recognized (Fig. 6). Figure 7 (upper row of plots) shows grayscale representations of the resulting clean maps (the lower row of plots shows electron density distributions further discussed in Sect. 4.4). The gray level (increasing from white to black, from zero to the maximum map value) corresponds to brightness, i.e., detected light per area. The figures refer to a gain of 0.1 (a) and subsequent redistribution of flux (b, see Sect. 4.3 below), and to a gain of 0.5 (c) and subsequent redistribution of flux (d). Pixels at the bottom of the image are symmetric to the projected orbit of the center of the A star and are stretched toward the bottom. For convenience, we cut these pixels off at this symmetry line. Since the areas of the various pixels on the map are not equal, small pixels may appear bright even if the total light emitted by the corresponding area may be small. There is, however, no trend in the maps for the brightest areas to predominantly populate small pixels. There are two main zones on the star that appear to contain active regions, one at the lower left, including a rather bright area near the limb and some further concentrations near the bottom of the stellar disk, and a second zone at the upper right, both on the disk and around the limb. All "active regions" appear to be modest in size.

4.3. Non-uniqueness; flux redistribution

Given any solution of pixel brightness on the clean map in the pixel coordinates (x_i, y_j) described in Sect. 4.2, $f(x_i, y_j)$,

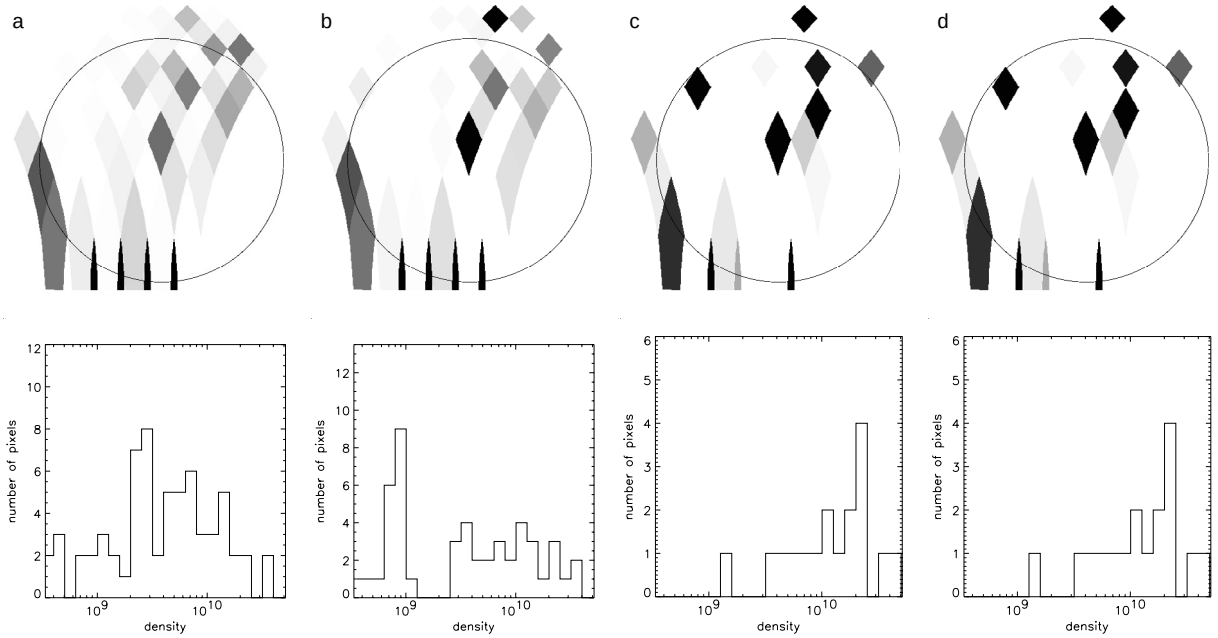

Fig. 7. X-ray brightness maps of α CrB resulting from the backprojection/CLEAN algorithm (upper row) and the corresponding electron density distributions of pixels (lower row). From left to right: **a)** CLEAN with gain 0.1; **b)** additional redistribution of flux; **c)** CLEAN with gain 0.5; **d)** additional redistribution of flux.

further solutions producing identical light curves can be generated.Consider, for example, pixel (x_i, y_j) with a flux f_{ij}; select another pixel (x_k, y_l) on the map with non-vanishing flux f_{kl}. The two pixels define two diagonally opposite corners of a rectangle in our bent coordinate system (x, y). The two other corners of the rectangle are then defined by the pixels (x_i, y_l) and (x_k, y_j). Choose an arbitrary amount of flux Δf that is smaller than each of f_{ij}, f_{kl}, and subtract it from the two initial pixels: $f'_{ij} = f_{ij} - \Delta f$, $f'_{kl} = f_{kl} - \Delta f$. Now add Δf to the two pixels at the other two corners of the rectangle, (x_i, y_l) and (x_k, y_j): $f'_{il} = f_{il} + \Delta f$, $f'_{kj} = f_{kj} + \Delta f$. The x and y projections remain identical by construction, and the corresponding light curve is thus unchanged. The large pixel sizes of the present method are ideally suited to investigate whether largely different flux distributions are possible. We have devised an algorithm that redistributes flux according to the above "diagonal rule". We present a solution in which we attempted to iteratively concentrate flux in the brightest pixels, as follows: We select the pair of brightest map pixels (x_i, y_j) and (x_k, y_l). We define a rectangle by using the two other corner points (x_i, y_l) and (x_k, y_j). We subtract some amount of flux Δf each from pixel (x_i, y_l) and (x_k, y_j), and add the same amount to pixels (x_i, y_j) and (x_k, y_l). If a redistribution is not possible according to this redistribution rule, the pixel pair next lower resp. next higher in flux is selected, until no further redistribution is possible according to this rule. This algorithm thus tends to concentrate as much flux as possible in a few bright sources at the cost of the fainter pixels.

The results are shown in Fig. 7 (plots *b* and *d* starting with the CLEAN maps *a* and *c* using gain = 0.1 and 0.5, respectively). There is no significant change in the map for $g = 0.5$, whereas for $g = 0.1$ much of the weaker flux has been contracted to brighter sources. The global distribution of bright regions remains similar.

4.4. Estimating densities

Since the clean map contains the fluxes (resp. the photon count rates) contributing to the light curve, we can estimate lower limits to the electron densities of the regions, as follows. For pixels close to the disk center, the third dimension is the height of the source. An estimate can be obtained using arguments given in Sect. 4.1 regarding the pressure scale height, or from characteristic size scales of bright sources derived in this paper. The size of the detected sources is determined by the time scales of the steep features in the light curve. As Fig. 1 shows, features *A*, *B*, *C*, and *D* all reveal a characteristic time scale of 300 s (the bin size). The distance the A-star limb projection advances on the G star during 300 s is approximately 5×10^9 cm. Depending on whether a source is close to the limb or close to the center of the G star disk, the size may represent the source height or the lateral extent. We have therefore adopted a characteristic depth of 5×10^9 cm over which we assume the plasma to be uniformly distributed. While this is probably a lower limit, the strong structuring of a corona by magnetic fields makes it unlikely that the entire pixel volume is uniformly filled by plasma, so that our standard height value is equivalent to larger effective heights. In any case, our density results scale inversely with the square root of the assumed height. We use these values also for the coarser pixels in the CLEAN reconstruction, for consistency.

From the spectral modeling described in Sect. 3, we obtain a count rate-to-luminosity conversion factor of 1.4×10^{29} erg s^{-1} for one ct s^{-1} in the combined PN+MOS1+MOS2 detectors. For a $T = 5$ MK plasma with the best-fit abundances reported above, the cooling rate per unit emission measure is $P(T) = 1.76 \times 10^{-23}$ erg s^{-1} cm^3 as modeled in XSPEC. We note that the Fe abundance is most critical for the estimate of the total emission measure, since much of the radiation at

this temperature is produced by Fe transitions. Therefore, an increase in the Fe abundance requires a smaller emission measure and vice versa. The cooling rate per emission measure is therefore dependent on the Fe abundance which has been determined with an uncertainty of about 10% although additional systematic uncertainties in the rather simple spectral fit could be possible. We changed the Fe abundance by 10% and held it fixed at the new value, while the other parameters were fitted as before. While the EM changed by about 7% and the temperature stayed about the same, the cooling rate changed by 5%.

The observed count rate from any given pixel can thus be converted into X-ray luminosity (using the stellar distance), and then to emission measure (using P). Adopting the pixel area and the pixel depth as given above, we find the emitting volume projecting into the pixel, and hence the electron density n_e (since $EM \approx n_\mathrm{e} n_\mathrm{H} V \approx 0.84 n_\mathrm{e}^2 V$). Note that the uncertainty of the density value due to the uncertainty of the Fe abundance is rather small, since the density scales with the square root of the emission measure. Figure 7 shows, in the lower row of plots, histograms of derived density values above 3×10^8 cm^{-3}. Values below 10^9 cm^{-3} are not likely to be significant as they correspond to rather faint pixels that are strongly influenced by the counting statistics in the light curve. We find a broad distribution between 10^9–10^{10} cm^{-3}, with a tail reaching up to 3×10^{10} cm^{-3}. The distributions are not the same for each reconstruction, which is little surprising given the different reconstruction conditions. Rather, the different distributions illustrate the range of allowed solutions for our various reconstruction methods (see also following sections). Overall, the distributions are reminiscent of the solar corona, but tend to reach to higher values (see, e.g., Landi & Landini 1998).

4.5. Maximum entropy reconstruction

This and the subsequent method (Sect. 4.6) use the full light curve at a resolution of 300 s. As before, we seek a flux distribution on the G star that describes the observed light curve. Whereas CLEAN concentrates the available flux in a number of point sources, the maximum entropy algorithm attempts to fit the observation with the flattest possible image. In this sense, the maximum entropy algorithm is an antipode to CLEAN, and the true brightness distribution is likely to lie between the two extremes.

Our maximum entropy method (MEM) selects among all images f_{ij} that are compatible with the observation, the one that minimizes the Kullback contrast ("relative entropy"; Eriksson et al. 1987)

$$K = \sum_{i,j} f_{ij} \ln \frac{f_{ij}}{f_{ij}^a} \tag{2}$$

with respect to the a priori image f_{ij}^a, which is unity within the admitted field of view ($R \le 1.25 R_*$) , and vanishes ($\ll$1) outside. The indices x_i, y_j again parameterize the retrieved image in our natural (curved) coordinates (x_i, y_j) (Fig. 3). The expression (2) is a measure for the information gain when the rough estimate f_{ij}^a is replaced by the more refined retrieval f_{ij}. Minimizing K thus introduces the least possible information

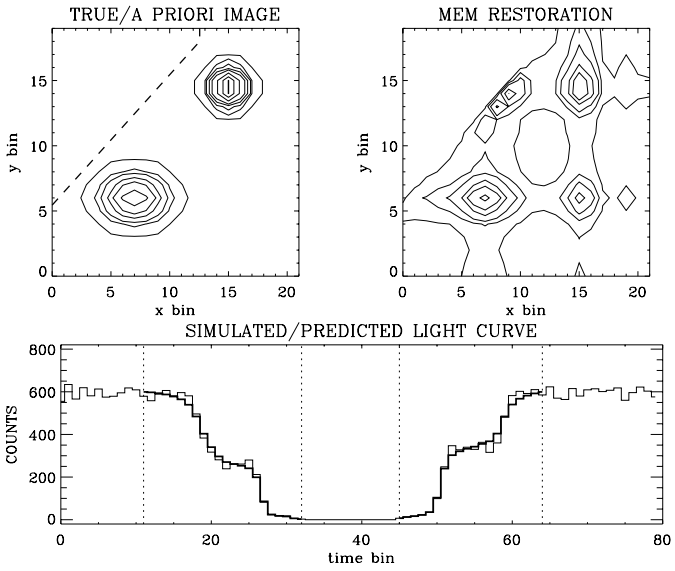

Fig. 8. Simulation of the maximum-entropy reconstruction of a test image (top left, solid) with a flat a priori image masking out the upper left triangular region (top left, dashed). The retrieved image (top right) predicts a light curve (bottom, bold line) which is consistent with the light curve of the test image (bottom, thin line) within statistical errors during the ingress and egress intervals (defined by the vertical lines). The retrieved image is flattest in the sense of minimizing the Kullback contrast with respect to the (flat) a priori image.

while being compatible with the observation. The contrast K is minimum if f_{ij} is proportional to f_{ij}^a (and $f_{ij} = f_{ij}^a$ if normalization is enforced) and thus flat inside the field of view; on the other hand, K is maximum if the whole flux is concentrated in a single pixel (x_i, y_j). Note that the position of this pixel does not affect K, nor does a permutation of pixels – the idea behind Eq. (2) is to choose the least biased image (rather than the smoothest one), based on the assumption that individual pixels represent independent degrees of freedom of the retrieved image (Tikochinsky et al. 1984). The case of constant f_{ij}^a is equivalent to the classical maximum-entropy method (e.g., Skilling & Brian 1984; Narayan & Nityananda 1986).

The compatibility with the observation is measured on the level of observed count rates, assuming that these follow the Poisson statistics in the approximate form

$$\chi^2 = \sum_k \frac{(F_k^* - F_k)^2}{F_k} \tag{3}$$

where F_k are the observed count rates in time bin k (for time t_k), and F_k^* are the corresponding count rates predicted from f_{ij}. The approximation (3) is justified by the fact that mostly $F_k \ge 15$ during the interesting time intervals of ingress and egress. Normalization is enforced by means of the constraint

$$N = \frac{\left(f^\mathrm{tot} - \sum_{ij} f_{ij} \right)^2}{f^\mathrm{tot}} \tag{4}$$

where the total flux f^tot of α CrB is taken from the light curve before and after total occultation. As suggested by

Fig. 1 (bottom), we set $f^{\rm tot} = 120$. The final algorithm minimizes the cost function

$$C = \chi^2 + \xi K + \eta N\,, \tag{5}$$

with K, χ^2, N given by Eqs. (2)–(4), respectively. The trade-off between the compatibility with the observation, normalization, and unbiasedness is determined by the Lagrange multipliers ξ and η, such that the reduced χ^2 is $\lesssim 1$, and normalization holds within a few percent. The minimization of C (Eq. (5)) is performed iteratively by a series of Newton/Marquardt steps.

As a benchmark, Fig. 8 shows the outcome of a MEM simulation with the true image consisting of two sources (top left, solid) and the a priori image f^a_{ij} which vanishes within the left upper triangular range (dashed). From the true image, one realization of Poisson distributed counts is constructed ("simulated light curve", lower panel), showing the ingress and egress due to covering and uncovering the true brightness distribution in x and y directions. The ingress and egress intervals are marked by dotted lines. From the simulated light curve, the maximum-entropy image (top right) is retrieved by minimizing Eq. (5). In both the true and retrieved images, the contours represent a set of fractions (0.01–0.99) of the maximum intensity of the true image. For comparison, the light curve predicted from the retrieved image is shown in the bottom panel (bold line). The predicted light curve is, by definition, monotonically decreasing (increasing) during ingress (egress), and can therefore not follow statistical secondary peaks of the simulated light curve. The final $\chi^2_{\rm red}$ is $\approx$0.8, and normalization is preserved within 3%. As can be noticed, the positions of the two sources are correctly retrieved, with their amplitudes somewhat flattened. The simulated light curve admits two spurious sources, one at (7, 14) and one at (15, 5). These spurious sources are placed at the intersections of the x- and y-projections of the true sources. The spurious source at (7, 14) is suppressed by the a priori image, but the one at (15, 5) is not. This is because the Kullback contrast does "see" symmetries, even if they were found likely to be artificial from inspection by eye. This is similar to the CLEAN result with small gain (Fig. 4).

The quality of the image reconstructions depends on the signal-to-noise ratio in the individual time bins. Since the method is iterative, the iteration can be terminated based on a reduced-χ^2 convergence criterion, measuring the count rate differences between model and observation. However, we invariably found that the convergence is slowest (and the contributions to χ^2 largest) at the times in the light curve where strong second derivatives are found (corresponding to times when active regions start becoming visible or start becoming eclipsed). Since these parts of the light curve contain crucial information on the extent of active regions, a global $\chi^2_{\rm red} \approx 1$ criterion introduces bias resulting in maps that are too smooth. We will therefore iterate our method until the model agrees closely with the observations in *all* bins.

However, iterating too closely to the given flux values introduces a jagged model light curve that fits statistical variations (steep gradients interchanging with plateaus), and the flux in the resulting map is contracted into too many small sources. As a practical limit, we require that the deviation between model and observation does not exceed 1σ in any time

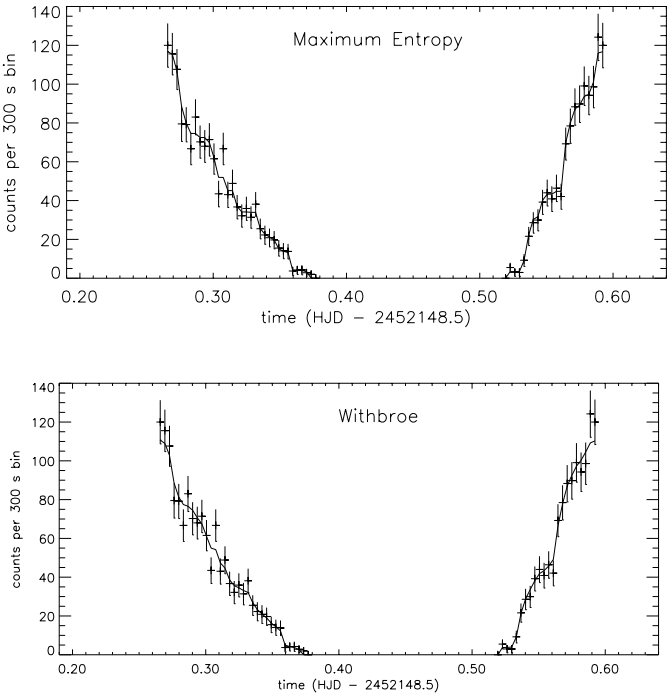

Fig. 9. Two examples showing data and fits for the maximum entropy algorithm (top) and the Withbroe method (bottom); the fit for the first version shown in Figs. 10 and 11, respectively, is shown. In the monotonic sections, the maximum deviation between fit and model is 1σ. The first and the last bin are set to 120 cts per bin, our adopted out-of-eclipse count rate.

bin in the monotonically falling (rising) parts of the observed ingress (egress) light curves. As explained above, those bins that do not follow the monotonicity because of counting statistics can principally not be fitted with arbitrary accuracy. To estimate the uncertainties in the resulting map, we subsequently repeat the image reconstruction after adding statistical noise to each light curve bin in agreement with its error bar, and finally we consider the average of three such maps.

Densities are derived as described in Sect. 4.4. The density distribution corresponding to the starting condition (same amount of light from each pixel) is narrowly peaked at $(8 \pm 1) \times 10^9$ cm^{-3} and is of little relevance for the iteration.

We show, as an example, the fit for the first version in Fig. 9 (top). We present in Fig. 10 three map reconstructions and the electron density distributions, the first relating to the input light curve as shown in Fig. 1, and the other two referring to versions with added Poisson noise. We also present the results from the co-added three maps.

The differences between different statistical realizations of the light curve are minor in Fig. 10. Densities are again found in the range between $10^9 - 3\times10^{10}$ cm^{-3}. The pixels with densities below 10^9 cm^{-3} are hardly reliable.

4.6. The "Withbroe" method

The "Withbroe" method (after Withbroe 1975) was extensively used by Siarkowski (1992), Siarkowski et al. (1996), and Preś et al. (1995) to reconstruct the structure of coronae of eclipsing

binary stars. It is formally related to maximum likelihood methods although the iteration and its convergence are methodologically different (Schmitt 1996). The method iteratively adjusts fluxes in a given set of bins based on the deviations between the model and the observed light curves. We follow the outline given in Siarkowski (1992) and briefly summarize the essential steps. At any given time t_k during the eclipse, the observed flux $F(t_k)$ is the sum of the fluxes f from all pixels that are unocculted:

$$F(t_k) = \sum_{i,j} f(x_i, y_j)\mathbf{m}(t_k, x_i, y_j) \quad (6)$$

where **m** is the "occultation matrix": it puts, for any given time t_k, a weight of unity to a pixel (x_i, y_j) if it is visible, and zero otherwise (our fine gridding does not necessitate intermediate weights for partially eclipsed pixels). Since $F(t_k)$ is given, we need to solve Eq. (6) for the 2D flux distribution, which is done iteratively as follows:

$$f^{n+1}(x_i, y_j) = f^n(x_i, y_j) \frac{\sum_k \frac{F_o(t_k)}{F_m^n(t_k)} \mathbf{m}(x_i, y_j)}{\sum_k \mathbf{m}(t_k, x_i, y_j)} \quad (7)$$

where $F_o(t_k)$ and $F_m^n(t_k)$ are, respectively, the observed flux and the model flux in the bin at time t_k, for the iteration step n. Initially, we assign equal amounts of X-ray flux to each pixel so that the sum corresponds to the observed total X-ray flux outside the eclipse. The iteration essentially corrects the brightness of a pixel according to the mismatch between model and observation in all time bins to which it contributes.

We use the same strategy for the termination of the iteration as discussed above for the Maximum Entropy method. The first and the last bin are again set to 120 cts per bin, our adopted out-of-eclipse count rate. A fit to the observed light curve closer than 1σ in each bin is typically achieved after a few hundred iterations. An example is shown in Fig. 9 (bottom). We present in Fig. 11 three map reconstructions and the electron density distributions, the first relating to the input light curve as shown in Fig. 1, and the other two referring to versions with added Poisson noise. We again also present the results from the co-added and averaged three maps. The brightness distributions are similar to those found in Sect. 4.5, although the method tends to converge to somewhat different shapes of the distributions and to lower average electron densities.

4.7. Variations of the fundamental parameters

Given the uncertainty in some system parameters, in particular the time of the secondary mid-eclipse, the inclination i, and the primary radius R_A, we investigated the influence of small variations on the resulting maps and electron density distributions. We arbitrarily use the first version of the Withbroe reconstruction (Fig. 11, left).

In a first case, we attempted to shift the secondary star in Fig. 3 to the left by reducing T_0 in Table 2 by 311 s, i.e., to a value close to that adopted by Schmitt (1998). The result is shown in Fig. 12a. It is very similar to our adopted solutions, indicating that the time shift is within the margins of error although the flux disappearing at the end of ingress (top right) is more compressed (the non-zero flux bins around 0.37 d in Fig. 1 are not correctly described if we keep the $1.25R_G$ limit for the X-ray sources; the bright feature at the extreme upper right is shifted inward toward the G star by one pixel row relative to the other features).

To optimize the coverage of the G star, we additionally decrease i by 0.7° to $i = 87.4°$. While the latter is outside the formal error range given in TP86, the map and the density distribution (Fig. 12b) are similar to our adopted solution (Fig. 11a), although the features are somewhat shifted relative to the G star.

Next, we restored the primary radius to the value given in TP86 (see Table 2). For optimal coverage, this required a substantial decrease of i to 86.9°, while T_0 is used as in the example above. Again, the reconstructed map and electron density distribution look similar (Fig. 12c).

Further, we may argue that our reconstructions tend to be biased toward small, high-density areas on the star since we fitted the light curves to within 1σ in each (monotonic) time bin, while estimating changes in the structure by varying the error bars afterwards. We therefore performed a fit using our initial parameters, but stopping the iteration as soon as a global reduced χ^2_{red} of 0.5 was achieved. The fit marginally describes the important features in the light curve while still not clearly fitting the locations with strong second derivatives. A χ^2_{red} exceeding 0.5 is not useful for these fits. This limiting case is shown in Fig. 12d. The results, including the electron density distributions, are again grossly similar to our original cases.

Lastly, we relaxed the constraint on the projected coronal radius ($R_C = 1.25R_G$) (while still cutting off the extended, ill-confined pixels south of the G star at the height of the A star center). Figure 13 compares reconstructions limiting R_C to $1.05R_G$, $1.1R_G$, $1.25R_G$, and $1.35R_G$. We note, however, that the first two radii are only marginally acceptable since the ingress time interval is slightly shorter than the observed interval, cutting off part of (for $1.1R_G$) or all of (for $1.05R_G$) the final non-zero ingress flux plateau at 0.36–0.38 d in Fig. 1. For the extended geometry for $1.35R_G$, flux is filled in above the G star (see Fig. 3 for reference) where the stellar limbs intersect at large heights, while laterally the large extension is not required by the ingress and egress time intervals. The solutions are thus biased by geometry, and flux is filled in above the star for geometrical reasons while solutions with all sources closer to or on the star are mathematically equally possible and physically more plausible.

Comparing Figs. 7, 10–13, we conclude that the reconstruction of the surface brightness images is rather robust within the margins of error of the fundamental parameters and the light curve. While the electron density distributions show variation between different reconstructions, the range of densities remains similar. The variation in the distributions partly reflects the bias inherent in the reconstruction methods. It illustrates the range of solutions given their principal non-uniqueness.

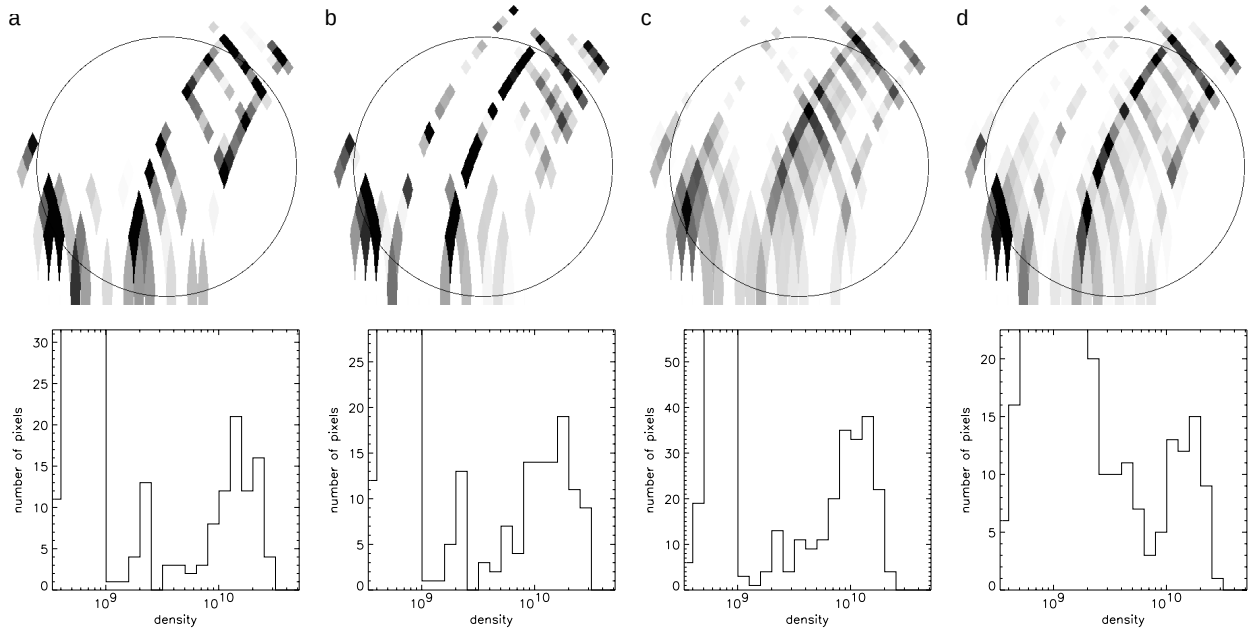

Fig. 10. X-ray brightness maps of α CrB resulting from the maximum entropy algorithm (upper row) and the corresponding electron density distributions of pixels (lower row). From left to right: **a)** fit to the initial light curve; **b, c)** two versions with noise added; **d)** all three maps averaged.

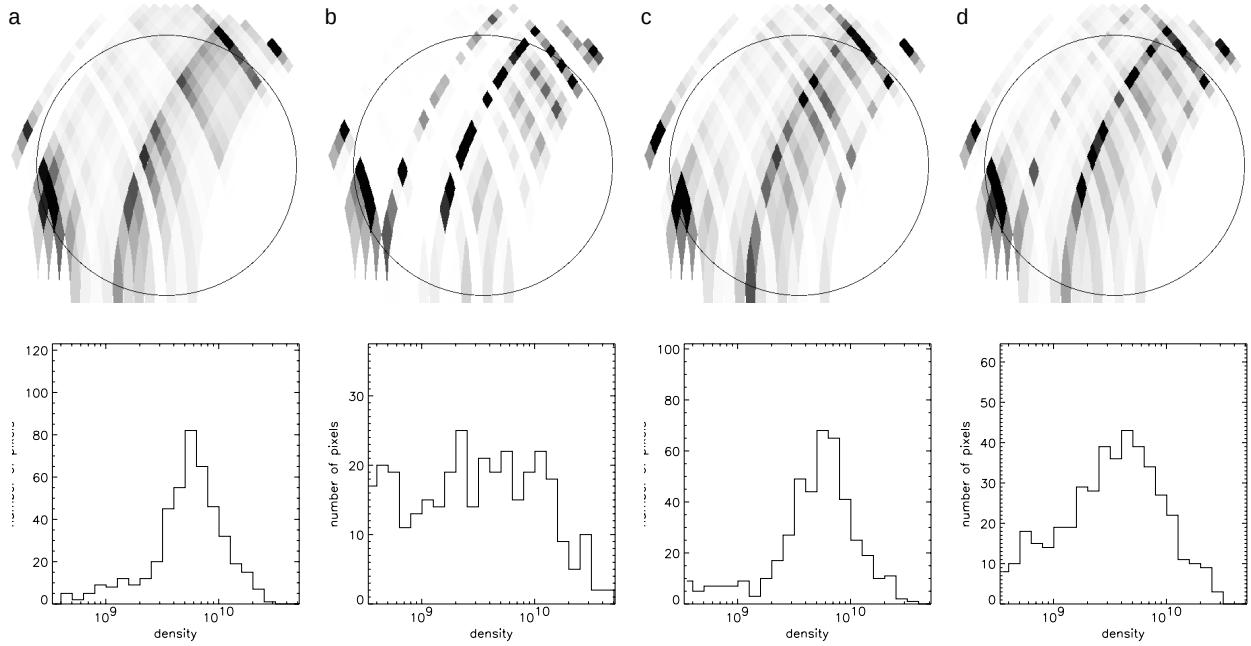

Fig. 11. X-ray brightness maps of α CrB resulting from the Withbroe algorithm (upper row) and the corresponding electron density distributions of pixels (lower row). From left to right: **a)** fit to the initial light curve; **b, c)** two versions with noise added; **d)** all three maps averaged.

5. Comments on the apsidal motion

Schmitt (1998) derived a value for the apsidal motion of the α CrB system from four ROSAT X-ray eclipse observations. We test whether the longer baseline of the time coverage now available can improve this result. While the primary eclipse can be well studied in the optical, leading to the primary period reported in Table 2, the optical secondary eclipse produces a drop of merely $0.02^{\rm m}$ (TP86). Obviously, the deep X-ray secondary eclipses are better suited. However, since the X-ray bright areas are not uniformly distributed on the star and the ingress and egress light curves are asymmetric, we are faced with considerable errors in our timing, as discussed earlier. We adopt the mid-eclipse time for our secondary observation as given in Table 2, $T_{\rm G}$ = 2452148.943. The error of this value can only grossly be estimated. The mean of the times of first and fourth (X-ray) contact is different from the mean of the times of second and third contact by about 1400 s. Inspection of Fig. 3 shows that a shift of the timing by one 800 s slice is critical since part of the observed eclipse may no longer occur

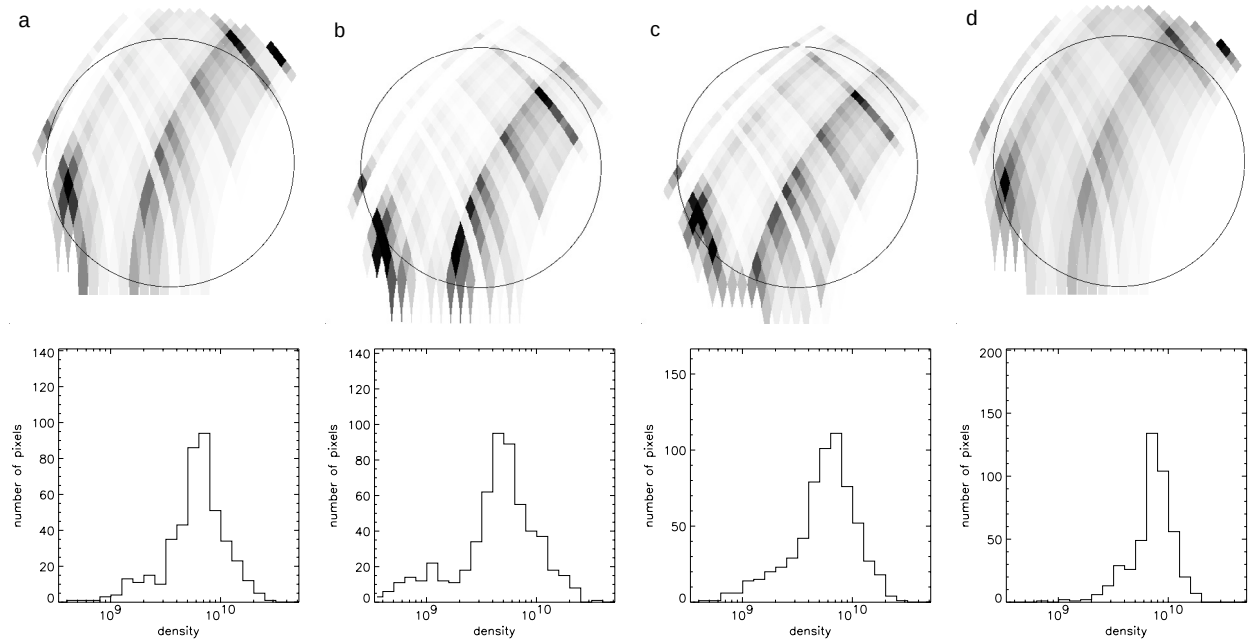

Fig. 12. X-ray brightness maps of α CrB resulting from the Withbroe algorithm (upper row) and the corresponding electron density distributions of pixels (lower row), after varying standard parameters. From left to right: **a)** Assuming a periastron passage 311 s earlier than adopted in this paper; **b)** same as **a)**, but also decreasing the orbit inclination by 0.7°; **c)** the same as **b)**, but adopting a primary radius as given by TP86 and an inclination of 1.2° smaller than adopted in this paper; **d)** a reconstruction using the standard parameters, but terminating the iteration when $\chi^2_{\rm red} = 0.5$.

reasonably close to the G star. A correction of the value of i may alleviate the problem, yet the literature value (TP86) is relatively narrowly confined. We conservatively estimate an absolute error of 800 s for our value of the secondary mid-eclipse time, also accounting for uncertainties in our adopted limiting radius of $1.25R_{\rm G}$ for the locations of bright X-ray sources. While Schmitt (1998) covered a time span corresponding to 97 orbit periods, the second *XMM-Newton* observation presented here extends this baseline to 192 periods. We note, however, that the timing error adopted above is between 3 and 5 times larger than the errors given by Schmitt (1998), and therefore our observation combined with his values will induce an uncertainty in $P_{\rm s}$ of the order 800 s/192 = 4.2 s, larger than the errors quoted in Schmitt (1998) and in fact about as large as his value for $P_{\rm s} - P_{\rm p}$. We conclude that the large asymmetry in our second light curve, originating from a strongly inhomogeneous distribution of X-ray bright regions at the time of our observation, does not improve previous estimates of the apsidal motion. We refrain from using the first light curve given its incompleteness and potential asymmetry, but note that further observations over a longer time baseline should be carried out.

6. Residual flux during the total X-ray eclipse?

During the time interval of the total X-ray eclipse, there may be residual X-ray flux owing to three potential sources: i) The A star itself may maintain a weak X-ray corona; ii) parts of the extended corona of the G star may still be visible; iii) charge exchange in a strong stellar wind may produce some X-rays (Wargelin & Drake 2002). The latter possibility is unlikely given the considerable distance of the star and the estimates given in Wargelin & Drake (2002). We investigated the PN image during the total eclipse (between 14.6 ks and 26.4 ks after the observation start, corresponding to the time range 0.38–0.51 d in Fig. 1, bottom. There was no residual flux visible in the corresponding detector image. The background level (see also Sect. 3) is 0.002 ct s^{-1} per PN source area. This value corresponds to 24 ± 5 cts collected in the respective area during total eclipse. Adopting a 3σ detection limit, the upper limit to the residual source count rate during eclipse is 0.0017 cts s^{-1}. This value is about 100 times lower than the out-of-eclipse source counts for the PN. We conclude that the residual luminosity of either the A star or the extended G star corona cannot exceed 6×10^{26} erg s^{-1} if the thermal model is the same as that derived for the G star emission.

7. Discussion and conclusions

We have reconstructed X-ray surface maps and coronal electron density distributions of the active young solar analog α CrB B, using three different methods. All reconstructions converge to similar surface brightness maps, and the results are robust against small variations of the system parameters. The robustness should be attributed to significant features in the light curve. We are now in a position to identify light curve features with active regions in the reconstructed maps: features *A* and *B* in Fig. 1 define the outline of the strong active region at lower left in the maps, near the limb of the G star. The strong increase *C* corresponds to the band diagonally running across the G star disk from lower left to upper right, close to the projected center. Feature *D* corresponds to a similar but weaker band displaced somewhat to the right, and also to the bright

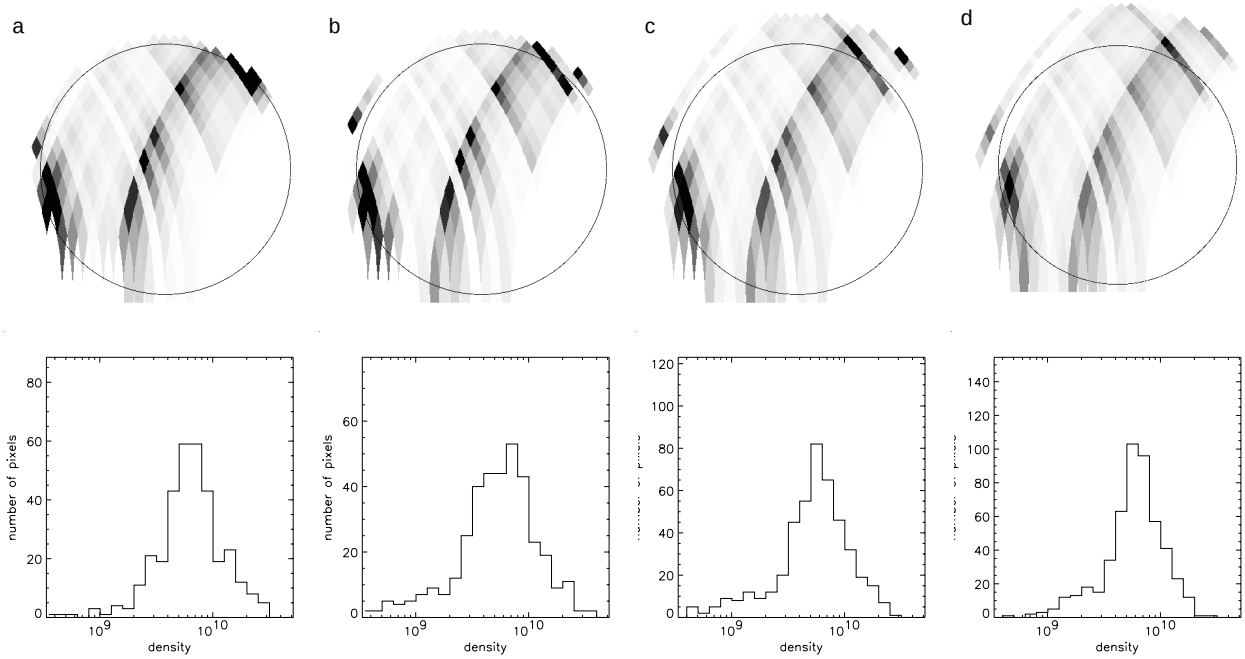

Fig. 13. X-ray brightness maps of α CrB resulting from the Withbroe algorithm (upper row) and the corresponding electron density distributions of pixels (lower row), for different limiting sizes of the coronal radius. From left to right: **a)** Coronal radius $R_C = 1.05R_G$; **b)** $R_C = 1.1R_G$; **c)** $R_C = 1.25R_G$; **d)** $R_C = 1.35R_G$.

source off the upper right secondary limb. The banded structure from lower left to upper right may partially be an artifact since the ingress light curve decays relatively smoothly below feature *A*, implying that there are no further individual strong sources to be localized along the slices of constant y.

Comparing the egress part of the two light curves in Fig. 1, it is striking that both are similarly short, even when the out-of-eclipse count rates are different. Our image reconstructions show that the egress curve does not cover the entire G star diameter. If this is a general feature, then it could suggest that the global arrangement of X-ray sources is elongated roughly along the direction of motion of the ingress primary limbs on the G star projection. This, in turn, would suggest that the X-ray active regions are arranged in a band that avoids regions in the upper left or lower right of the G star disk, which would (by the solar analogy) most likely correspond to the areas around the stellar poles. In that case, the rotation axis would be approximately perpendicular to the egress limb cuts, i.e., pointing to the upper left in our maps. Such an orientation would be highly unusual as it implies that the rotation axis were strongly inclined to the axis of the orbit. This hypothesis can be tested only with additional observations of the full eclipse.

We note that we have not considered the possible changes in position of some of the X-ray sources due to the surface rotation during our observation. If we adopt a rotation period of 8 d, then a source projected onto the center of the G star disk may move by about 9% of the star's diameter while being eclipsed. This motion will not result in a source smearing in our maps but in a shift of the source compared to its true place. Consider, in Fig. 3, a rotation axis that is parallel to the axis of the orbit and a sense of rotation that is the same way as the orbital motion. Then, the egress limbs pick up the source somewhat later than compared to a stationary source. The intersection of the ingress slice with the delayed egress slice moves the source downward. This effect becomes smaller the closer the source is to the stellar limb. Since we do not know a priori which source is close to the disk center and since the orientation of the rotation axis is unknown, we have not modeled rotational effects but note that, apart from small shifts of some sources, the principal results should not be affected.

Although our map reconstructions are principally non-unique, all methods converge to somewhat similar X-ray source distributions. The X-ray brightness distribution is reminiscent of the Sun's despite an X-ray luminosity exceeding the active Sun's by a factor of ≈30. However, a large part of the G star surface area reveals sources in which (using our parameters) the electron density exceeds 10^9 cm^{-3}. For example, in Fig. 11a, essentially all shaded areas on and around the G star imply such densities. This is rather different from the Sun since densities of this magnitude are attained in active regions, which cover only a modest fraction of the solar surface even at coronal heights (e.g., Landi & Landini 1998). The densest regions in our maps exceed 10^{10} cm^{-3}, with extreme values found around $2\text{–}3\times10^{10}$ cm^{-3} consistently in all reconstructions. We emphasize that these values depend on our assumptions on the depth of the projected sources, for which we can give no definitive estimates, but argued that a value of 5×10^9 cm is reasonable. Electron densities may be higher if the filling factor of bright material within the pixel volumes is less than one.

To return to our initial question on the cause of the increased X-ray luminosity in magnetically active stars, our tentative answer is a diplomatic one: from our maps, we infer a large coverage with dense (>10^9 cm^{-3}) sources, but also extreme density values exceeding 10^{10} cm^{-3} in the brightest

areas. At the same time, the average corona is much hotter than the dominant plasma in the non-flaring Sun; from spectral fits, we infer $T \approx 5$ MK. These three findings can be accounted for by a simple picture involving interactions of magnetic fields as discussed in Güdel et al. (1997) (see also discussion in Drake et al. 2000). As the magnetic dynamo increases toward more active stars, the surface filling factor of strong magnetic fields increases, increasing also the volume filling factor of closed loops in the corona. As the magnetic loops are packed closer together than on the Sun, they interact more frequently, producing a higher rate of field annihilation and reconnection, thus generating flares at a higher rate. These energy release events liberate magnetic energy and heat chromospheric plasma, evaporating it by overpressure into the magnetic loops. One thus expects both a larger average density in the corona and a higher temperature if the flare rate is higher. Such a scenario is well supported by our findings. Increased densities and temperatures both are, in this picture, a natural consequence of a denser packing of magnetic fields in the corona, induced by a more efficient dynamo in stars with more rapid rotation.

Some large areas on the star are, however, X-ray faint, in particular at the lower right, but also at the upper left in our images. The lower right part is poorly covered by the cut-off egress part. As we have argued in Sect. 3, it is likely that we observed the full egress since the final flux is equal to the flux observed before eclipse. The information in the light curve during the high radiation episode after the MOS turn-off is unreliable, with a rapidly increasing background level. An additional increase of 15% beyond the full count rate level may be possible although we refrain from modeling this further. It would fill in some modest flux contributions in the lower right part of the stellar surface. If the low-brightness areas are real, then, in the solar analogy, they correspond either to areas with little concentration of active regions or bright spots, or to coronal holes. These areas may be important for the generation of the fast stellar wind (in analogy to the fast solar wind), and therefore contribute significantly to the stellar spin-down due to angular momentum loss.

As a by-product, our data obtained during the full eclipse allow us to put constraints on the X-ray luminosity of the A star or an extended G star corona. We find upper limits of about 6×10^{26} erg s^{-1} (0.1–10 keV) for such emission. Although the eclipse light curve could be used to study the periastron advance further, the strong asymmetry found in our light curve prevents us from improving on previous results. Future observations obtained over a larger period of time are required.

Acknowledgements. We thank the referee for constructive comments that helped improve this paper. MG and MA acknowledge support from the Swiss National Science Foundation (grant 2000-058827, and fellowship 81EZ-67388 to MA), from the Swiss Academy of Natural Sciences, and from the Swiss Commission for Space Research. SRON is supported financially by NWO.

References

Anders, E., & Grevesse, N. 1989, Geochim. Cosmochim. Acta, 53, 197
Arnaud, K. A. 1996, in Astronomical Data Analysis Software and Systems V, ed. G. Jacoby, & J. Barnes (San Francisco: ASP), ASP Conf. Ser., 101, 17
Audard, M., Güdel, M., Drake, J. J., & Kashyap, V. 2000, ApJ, 541, 396
Audard, M., Güdel, M., & Mewe, R. 2001, A&A, 365, L318
Ayres, T. R. 1997, JGR, 102, E1, 1641
Benz, A. O., Alef, W., & Güdel, M. 1995, A&A, 298, 187
Benz, A. O., Conway, J., & Güdel, M. 1998, A&A, 331, 596
Butler, C. J., Rodonò, M., Foing, B. H., & Haisch, B. M. 1986, Nature, 321, 679
den Herder, J. W., Brinkman, A. C., Kahn, S. M., et al. 2001, A&A, 365, L7
Dorren, J. D., & Guinan, E. F. 1994, ApJ, 428, 805
Dorren, J. D., Güdel, M., & Guinan, E. F. 1995, ApJ, 448, 431
Drake, J. J., Brown, A., Patterer, R. J., et al. 1994, ApJ, 421, L43
Drake, J. J., Peres, G., Orlando, S., Laming, J. M., & Maggio, A. 2000, ApJ, 545, 1074
Eriksson, K.-E., Lindgren, K., & Mansson, A. 1987, Structure, Context, Complexity, Organisation (Singapore: World Scientific Publishing)
Feldman, U., Laming, J. M., & Doschek, G. A. 1995, ApJ, 451, L79
Güdel, M. 1997, ApJ, 480, L121
Güdel, M., Audard, M., Briggs, K., et al. 2001a, A&A, 365, L336
Güdel, M., Audard, M., Magee, H., et al. 2001b, A&A, 365, L344
Güdel, M., Audard, M., Kashyap, V., Drake, J. J., & Guinan, E. F. 2003, ApJ, 582, 423
Güdel, M., Guinan, E. F., & Skinner, S. L. 1997, ApJ, 483, 947
Güdel, M., Guinan, E. F., & Skinner, S. L. 1998, in Tenth Cambridge Workshop on Cool Stars, Stellar Systems and the Sun, ed. R. A. Donahue, & J. A. Bookbinder (San Francisco: ASP), 1041
Güdel, M., Schmitt, J. H. M. M., Benz, A. O., & Elias, N. M. II. 1995, A&A, 301, 201
Gunn, A. G., Migenes, V., Doyle, J. G., Spencer, R. E., & Mathioudakis, M. 1997, MNRAS, 287, 199
Jansen, F., Lumb, D., Altieri, B., et al. 2001, A&A, 365, L1
Kashyap, V., Drake, J. J., Güdel, M., & Audard, M. 2002, ApJ, 580, 1118
Kopp, R. A., & Poletto, G. 1993, ApJ, 418, 496
Kürster, M., Schmitt, J. H. M. M., Cutispoto, G., & Dennerl, K. 1997, A&A, 320, 831
Landi, E., & Landini, M. 1998, A&A, 340, 265
Lim, J., White, S. M., & Cully, S. L. 1996, ApJ, 461, 1009
Mason, K., Breeveld, A., Much, R., et al. 2001, A&A, 365, L36
Meeus, J. 1988, Astronomical Formulae for Calculators (Willmann-Bell)
Mutel, R. L., Lestrade, J.-F., Preston, R. A., & Phillips, R. B. 1985, ApJ, 289, 262
Mutel, R. L., Molnar, L. A., Waltman, E. B., & Ghigo, F. D. 1998, ApJ, 507, 371
Narayan, R., & Nityananda, R. 1986, ARA&A, 24, 127
Ness, J.-U., Mewe, R., Schmitt, J. H. M. M., et al. 2001, A&A, 367, 282
Pallavicini, R., Golub, L., Rosner, R., Vaiana, G. S., Ayres, T., & Linsky, J. L. 1981, ApJ, 248, 279
Parker, E. N. 1988, ApJ, 330, 474
Peres, G., Orlando, S., Reale, F., Rosner, R., & Hudson, H. 2000, ApJ, 528, 537
Perryman, M. A. C., and the *Hipparcos* Science Team 1997, The *Hipparcos* and *Tycho* Catalogues (ESA report SP-1200; Noordwijk: ESA)
Preś, P., Siarkowski, M., & Sylwester, J. 1995, MNRAS, 275, 43
Radon, J. 1917, reprinted in 1983, Proc. Symp. in Appl. Math., 27, 71

Schmitt, J. H. M. M. 1996, in Stellar Surface Structure, ed. K. G. Strassmeier, & J. L. Linsky (Dordrecht: Kluwer), IAU Symp., 176, 85
Schmitt, J. H. M. M. 1998, A&A, 333, 199
Schmitt, J. H. M. M., & Kürster, M. 1993, Science, 262, 215
Siarkowski, M. 1992, MNRAS, 259, 453
Siarkowski, M., Preś, P., Drake, S. A., White, N. E., & Singh, K. P. 1996, ApJ, 473, 470
Skilling, J., & Brian, R. K. 1984, MNRAS, 211, 111
Strüder, L., Briel, U. G., Dennerl, K., et al. 2001, A&A, 365, L18
Tikochinsky, Y., Tishby, N. Z., & Levine, R. D. 1984, Phys. Rev. Lett., 52, 1357
Tomkin, J., & Popper, D. M. 1986, AJ, 91, 1428 (TP86)
Turner, M. J. L., Abbey, A., Arnaud, M., et al. 2001, A&A, 365, L27
Vaiana, G. S., & Rosner, R. 1978, ARA&A, 15, 363
Vilhu, O. 1984, A&A, 133, 117
Vilhu, O., & Walter, F. M. 1987, ApJ, 321, 958
Volkov, I. M. 1993, IBVS, 3876
Walter, F. M. 1981, ApJ, 245, 677
Wargelin, B. J., & Drake, J. J. 2002, ApJ, 578, 503
White, N. E., Shafer, R. A., Horne, K., Parmar, A. N., & Culhane, J. L. 1990, ApJ, 350, 776
Withbroe, G. L. 1975, Sol. Phys., 45, 301